



Atomic level dispersed nickel coupled with silver nanoparticle to boost the efficiency of CO₂ conversion to CO via spin electrons regulation

Zibo Zhao ^{a,1}, Liu Lin ^{b,1}, Youxuan Ni ^{b,1}, Lin Jin ^a, Lanlan Feng ^a, Yuwen Wang ^a, Yajuan Wei ^{a,b,*}, Jingbo Zhang ^{a,**}, Jun Chen ^{b,***}

^a Key Laboratory of Inorganic-Organic Hybrid Functional Material Chemistry, Ministry of Education, Tianjin Key Laboratory of Structure and Performance for Functional Molecules, College of Chemistry, Tianjin Normal University, Tianjin 300387, China

^b Key Laboratory of Advanced Energy Materials Chemistry (Ministry of Education), College of Chemistry, Nankai University, Tianjin 300071, China



ARTICLE INFO

Keywords:

Multi-scale active sites
Atomic-level
Ni₃
Ag nanoparticles
Spin electrons regulation

ABSTRACT

Modulating the electronic configuration by coupling multi-scale active sites for electrocatalytic conversion of CO₂ to CO is extremely challenging in terms of structural analysis and mechanism elucidation. Herein, a catalyst NiAD/AgNPs@CN with both atomic-level dispersed Ni and Ag nanoparticles on N-doped carbon substrate has been designed to reveal the true active sites and catalytic mechanism in complex materials. NiAD/AgNPs@CN exhibits CO Faraday efficiency (FE_{CO}) of 99.97% at -0.88 V (vs. RHE) in H-type cell and 91.77% FE_{CO} with a high current density of 79.70 mA/cm² in flow cell. DFT calculations show that the tiny change in the energy level of spin electrons at atomic sites has a significant impact on the CO₂ activation. The regulation of atomic Ni on Ag sites is the main reason for improving CO₂RR performance. This work gives a new understanding on the catalytic mechanism of composite materials structured by atomic-level dispersed metal and nanoparticles.

1. Introduction

Electrochemical CO₂ reduction reaction (CO₂RR) has been considered as an effective technology to alleviate a series of environmental and energy crises by activating inert CO₂ molecules and reducing them into more cost-effective chemical fuels.^[1–6] It is well known that CO₂RR involves a wide distribution of products, including C₁ products (carbon monoxide, formic acid, methanol, and methane) and C₂ products (acetic acid, ethanol, ethylene, and ethane).^[7–11] Among the multitudinous products, CO produced through a two-electron transfer process, is considered to be the most economical reduction product, due to their high added value per KJ of electrical energy input.^[12–16] At the same time, CO is a vital raw material of Fischer-Tropsch synthesis, which has great potential commercial value in industrial applications.^[17–19] Therefore, it is attractive to design highly efficient catalysts for CO₂RR that convert CO₂ to CO. However, subject to the occurrence of competitive hydrogen evolution reaction (HER), it is necessary to design and synthesize efficient CO₂RR catalysts with high selectivity and

stability aiming at the CO₂-to-CO mechanism.^[20–24]

Recently, there have been two widely accepted mechanisms for converting CO₂ to CO via CO₂RR. One mechanism (I) involves four steps: (1) * + CO₂ + e⁻ → *CO₂⁻, (2) *CO₂⁻ + H⁺ → *COOH, (3) *COOH + H⁺ + e⁻ → *CO + H₂O, (4) *CO → CO + *. The other mechanism (II) mainly involves three steps: (1) * + CO₂ + H⁺ + e⁻ → *COOH, (2) *COOH + H⁺ + e⁻ → *CO + H₂O, (3) *CO → CO + *.^[25,26] Converting CO₂ to CO involves a two-electrons and two-protons reaction process, generation of the reaction intermediate *COOH, and desorption of *CO are the main rate-limiting step. The major difference between the two mechanisms is the activation of CO₂. CO₂ molecules are usually first adsorbed and activated on the surface of the catalyst. Mechanism (I) is a decoupled electron and proton transfer process (Eqs. (1) and (2)) that begins with the formation of CO₂⁻ radical anions at the electrode surface. It requires strong electron transfer between active sites and CO₂ molecules to overcome the high energy barriers in this mechanism. While, this strong electron transfer often results in highly active sites being poisoned by reaction intermediates and products, thus reducing the overall

* Corresponding author at: Key Laboratory of Inorganic-Organic Hybrid Functional Material Chemistry, Ministry of Education, Tianjin Key Laboratory of Structure and Performance for Functional Molecules, College of Chemistry, Tianjin Normal University, Tianjin 300387, China.

** Corresponding authors.

E-mail addresses: yj_wei@tjnu.edu.cn (Y. Wei), hxyzjb@tjnu.edu.cn (J. Zhang), chenabc@nankai.edu.cn (J. Chen).

¹ Authors Zibo Zhao, Liu Lin and Youxuan Ni contributed equally to this work.

reactivity. Clearly, the step of $^* + \text{CO}_2 + \text{e}^- \rightarrow ^*\text{CO}_2$ in mechanism (I) is unfavorable. Mechanism (II) is a coupled proton-electron transfer process that generates $^*\text{COOH}$ intermediates in the first step. The energy barriers of $^*\text{COOH}$ intermediates formation are relatively lower and can be achieved when the active sites interact with CO_2 molecules with moderate intensity, which is conducive to the occurrence of subsequent reaction steps. The reaction path of $\text{CO}_2 \rightarrow \text{CO}$ mainly depends on the interaction between the active sites and CO_2 molecules. Therefore, how to adjust the energy level structure of the active sites to make them have suitable adsorption strength for CO_2 molecules, so as to drive the reaction to proceed according to the mechanism (II), is a huge challenge, and is also the key to improving the activity of CO_2RR .

In recent years, single-atom catalysts (SACs) have been widely recognized as effective catalysts in the field of CO_2RR .^[27,28] Among them, nickel-based SACs are acknowledged as the most promising catalysts for the conversion of CO_2 to CO .^[29–31] However, Ni SACs often include mixed structures (such as nanoparticles or clusters) and different coordination environments due to the challenge of precise synthesis. Although most of the particles/clusters can be cleaned by pickling, a very small number of particles/clusters or multi-atomic sites also have an impact on the reaction. The reaction mechanism that ignores the impact of clusters and multi-atomic sites may not be accurate, which greatly limits the elaboration of the CO_2RR mechanism.^[32,33] In fact, nanoparticles or clusters will interact with the active site, thus producing activity at the interface which is different from that of the simple atomic site. A few such studies have been reported but mainly focus on the regulation of the atomically dispersed active sites by clusters or particles, often ignored the direct interaction between clusters or nanoparticles themselves with carbon dioxide molecules.^[34–37] Therefore, we focus on the direct interaction between nanoparticles and atomic-dispersed nickel active centers to discover the real reaction sites for CO_2RR and bring a basis for the designation of high-efficiency CO_2RR catalysts.

To better distinguish the role of atomic Ni sites and nanoparticles or clusters in catalysis, we choose another metal to build a composite structure. Various nanoparticles (Pd, Au, Ag, etc.) show good selectivity and activity in the process of $\text{CO}_2 \rightarrow \text{CO}$.^[38–43] Compared to palladium and gold, silver has been considered an ideal material for transforming CO_2 into CO for commercial application due to the relatively lower price and more abundant earth reserves.^[44,45] Silver can activate CO_2 efficiently and facilitate $^*\text{CO}$ desorption, thus contributing to $\text{CO}_2 \rightarrow \text{CO}$ conversion in CO_2RR .^[46,47] Therefore, we select Ag to construct nanoparticles and composite with atomic Ni sites.

The deeper reason for selecting silver is that the mechanism of CO_2RR on Ag nanoparticles and SACs may be significantly different. It has been reported that the reaction path of silver catalysts mostly occurs according to mechanism (II). The coupled proton-electron transfer process occurs on Ag to generate $^*\text{COOH}$ intermediates in the first step.^[48,49] However, most Ni SACs can effectively activate CO_2 molecules and make CO_2 reduce to CO following mechanism (I).^[50–52] Liu group established a Ni SACs model catalyst with well-defined Ni-N₄ sites which demonstrates that the rate-determining step of the $\text{CO}_2 \rightarrow \text{CO}$ was determined to be $^*\text{CO}_2 + \text{H}^+ \rightarrow ^*\text{COOH}$.^[53] That means Ni SACs site firstly activates CO_2 molecules to form $^*\text{CO}_2$ and adsorb hydrogen to achieve the proton-electron coupling process. We speculate that the different CO_2RR mechanisms between Ag particles and Ni SAC mainly result from the different adsorption strengths between Ag and Ni SAC with CO_2 molecules. It is very worthwhile to explore the modulation of the two and unveil the essential catalytic activity and reaction mechanism when they contact each other. On the one hand, under the action of Ag, the electronic conformation of atomic Ni sites may change, and then adjust the intensity of interaction between Ni and CO_2 molecules, so that push the reaction proceeding according to mechanism (II) and reduce the reaction barrier and accelerate the reaction kinetics from the thermodynamics. On the other hand, the Ag site is also affected by the Ni site, which leads to a change of its reaction activity and even the reaction

mechanism.

Based on the above discussion, herein, we developed a N-doped carbon (CN) supported catalyst with atomic level dispersed Ni active sites (NiAD) surrounding Ag nanoparticles (NiAD/AgNPs@CN) via a carbon layer coating strategy to enhance the CO_2RR performance. The synthesized NiAD/AgNPs@CN shows a FE_{CO} of nearly 100% at a moderate potential -0.88 V (vs. RHE) and displays a wide potential window range ($-0.68 \sim -1.08$ V vs. RHE) with the FE_{CO} exceeding 90% in H-type cell. In the flow cell, at -0.88 V (vs. RHE), the FE_{CO} reaches the maximum value ($> 90\%$) with a high current density of 79.70 mA/cm^2 , indicating a good prospect for industrial application. The reaction path at the atomic level and the micro process of electrocatalytic CO_2 to CO were deeply revealed by experiment and DFT calculation. DFT results show that spin electron energy levels change subtly after contacting between Ni sites and Ag sites, resulting in a qualitative change in the adsorption strength of the two with CO_2 molecules. The obvious weakening of CO_2 absorptive intensity on Ni sites caused by Ag sites results in the reaction mechanism on the Ni site changes significantly. In contrast, the atomically dispersed nickel sites effectively improve the adsorption of CO_2 on silver nanoparticles, thus greatly reducing the energy barrier of the generated $^*\text{COOH}$ intermediates and desorption $^*\text{CO}$, thus improving the catalytic activity. The nature of the interaction between atomic-scale dispersed metal sites and metal nanoparticles, as well as its influence on the catalytic performance and mechanism of CO_2RR , proposed in this paper, provides the possibility to explain the reaction mechanism in complex materials and guides the direction of building high-performance catalysts with composite structures.

2. Experimental section

2.1. Materials

Ammonium chloride (NH_4Cl , $\geq 99.5\%$) was purchased from Tianjin Wind Boat Chemical Reagent Technology Co., Ltd; Dicyandiamide (DCD, 99%) and silver nitrate (AgNO_3 , 99.8%) were purchased from Aladdin; nickel chloride (NiCl_2 , 99%) was obtained from 3 A Chemicals; glucose ($\text{C}_6\text{H}_{12}\text{O}_6 \cdot \text{H}_2\text{O}$, AR) was purchased from Tianjin Guangfu Technology Development Co., Ltd; potassium bicarbonate (KHCO_3 , 99.7–100.5%) was purchased from Alfa Aesar (China) Chemical Co., Ltd.

2.2. Synthesis of catalysts

2.2.1. Preparation of AgNPs@CN catalyst

10 g NH_4Cl , 2 g Dicyandiamide, 0.2 mmol AgNO_3 were dissolved in 30 mL deionized water and freeze-dried, then 4 g freeze-dried powder was put into a crucible and heated to 550°C in the argon atmosphere at a rate of $5^\circ\text{C}/\text{min}$ for 2 h. The brown powder was obtained and ready for use. Then the 300 mg brown powder was ultrasonically dispersed in 21 mL 0.3 M glucose solution for 2 hours, then transferred to the 100 mL stainless steel hydrothermal reactor, reacted at 180°C for 10 h, cooled to room temperature, washed 5 times with deionized water and ethanol respectively, and then vacuum dried at 50°C overnight. The dried powder was transferred to the crucible again, and the temperature was raised to 1000°C at a rate of $5^\circ\text{C}/\text{min}$ in a tube furnace in argon atmosphere and kept for 1 hour. Finally, the collected product was named AgNPs@CN.

2.2.2. Preparation of NiAD/AgNPs@CN catalyst

10 g NH_4Cl , 2 g Dicyandiamide, 0.1 mmol AgNO_3 , 0.2 mmol NiCl_2 were dissolved in 30 mL deionized water and freeze-dried, then 4 g freeze-dried powder was put into a crucible and heated to 550°C in argon atmosphere at a rate of $5^\circ\text{C}/\text{min}$ for 2 h. Then, the brown powder was obtained and ready for use. 300 mg brown powder was ultrasonically dispersed in 21 mL 0.3 M glucose solution for 2 hours and then transferred to 100 mL stainless steel hydrothermal reactor, reacted at

180°C for 10 h, washed 5 times with deionized water and ethanol respectively, and then vacuum dried at 50°C overnight. The dried powder was transferred to the crucible again and raised to 1000°C at a rate of 5°C/min in a tube furnace in argon atmosphere and kept for 1 hour. Finally, the collected product was named NiAD/AgNPs@CN.

NiAD/AgNPs@CN is an optimized material with the best performance of CO₂RR by adjusting different silver-nickel ratios. The other two samples with different Ag/Ni proportions were named as NiAD/AgNPs@CN-1, and NiAD/AgNPs@CN-2, respectively. The procedure is similar to that of NiAD/AgNPs@CN, except that the feed ratio of AgNO₃ and NiCl₂ is changed to 1:1 and 2:1, respectively. For comparison, the similar tests with NiAD/AgNPs@CN of the two catalysts were also carried out, the results were shown in Figure S1-S3.

2.2.3. Preparation of NiAD@CN, and NiNPs@CN catalysts

For the synthesis of NiAD@CN, NiNPs@CN samples, the process is basically the same as that of AgNPs@CN, except that 0.2 mmol AgNO₃ can be replaced with the same amount of NiCl₂ and 0.4 mmol NiCl₂, respectively.

2.2.4. Preparation of CN catalyst

For the synthesis of CN sample, the steps are basically the same as those of the above six materials, except that no metal salt precursors are added.

The elemental composition of the catalysts has been obtained in Table S1.

2.3. Materials characterization

X-ray powder diffraction (XRD, D8 ADVANCE of Bruker Inc.) is applied to determine the crystal structure. The morphology and element distribution are contributed by Scanning electron microscope (SEM, FEI Nova Nano SEM 230 of American FEI Inc.), Field emission transmission electron microscope (FETEM, Themo Fisher SCIENTIFIC Talos F200X), and Aberration-corrected high-angle annular dark-field scanning transmission electron microscopy (ACHAADF-STEM, Spectra 300). The chemical composition and electronic valence of elements are determined by X-ray photoelectron spectrometer (XPS, Shimadzu AXIS-ULTRA-DLD). X-ray Absorption Spectroscopy (XAS) experiments on Ni K-edge were carried out at beamline 1W1B of the Beijing Synchrotron Radiation Facility. The content of elements is analyzed by inductively coupled plasma emission spectroscopy (ICP-OES, Agilent 720). The liquid products are detected by Nuclear magnetic resonance hydrogen spectrometer (¹HNMR, AVANCE III of Bruker Inc.), and the gas products are monitored by Gas Chromatography (Shimadzu GC-2010 Plus).

2.4. Electrochemical test

2.4.1. Electrochemical characterization

All the electrochemical tests were carried out on the electrochemical workstation (CHI660E). The electrolytic cell is a traditional airtight two-chamber H-type cell with three-electrode structure, the opposite electrode is platinum, the reference electrode is Ag/AgCl electrode filled with KCl saturated solution, and the working electrode is coated with carbon paper with uniformly dispersed catalyst (1×1 cm²). The electrolyte is CO₂-saturated 0.1 M KHCO₃ solution. The preparation process of the working electrode is as follows: 2 mg catalyst and 80 μL Nafion are added to the mixed solution composed of 230 μL ethanol and 690 μL secondary water, ultrasonic dispersion is dispersed to the shape of ink, and then 100 μL dispersion is evenly dripped to the carbon paper 1×1 cm² area.

2.4.2. Electrochemical measurements

Before each CO₂RR test, CO₂ gas (99.999%, liquid air) is first used to purge for 30 min. During the test, the CO₂ gas is continuously vented, so that the CO₂ concentration in the electrolyte is always in a saturated

state.

All the test potentials can be based on the Nernst Eq. (1):

$$E \text{ (vs.RHE)} = E \text{ (vs.Ag/AgCl)} + 0.210V + 0.0591 \times pH \quad (1)$$

At room temperature, Ar or CO₂ gas was used to purge the electrolyte for 30 min, and then the LSV curve was obtained at the scanning rate of 10 mV/s. By applying an AC voltage with a vibration amplitude of 5 mV, the electrochemical impedance spectra of a series of catalysts were measured in the 0.1 Hz ~1000 KHz frequency range. In the range of -0.1 V ~ 0.1 V potential, the CV curves were obtained by changing the scanning rate from 10 mV/s to 50 mV/s, and the electrochemical double layer capacitance (C_{dl}) of the catalysts were calculated according to the test results of the CV curves.

The Faraday efficiency (FE) of gas phase products is calculated by Eq. (2):

$$FE = \frac{nFVPv}{RTI_{total}} \times 100\% \quad (2)$$

Where *n* represents the number of electron transfers in the product formation process (for CO and H₂, *n* = 2), *F* represents the Faraday constant (96485 C/mol), *V* (mL/min) represents the gas flow rate monitored by the flow meter at the outlet of the electrolytic cell at room temperature and ambient pressure, *P* (Pa) is the pressure at room temperature, *v* (vol%) represents the volume concentration of the product detected by gas chromatography.

The turnover frequency (TOF) of CO is calculated by Eq. (3):

$$TOF = \frac{J_{CO}M_{Ni}}{nFm_{cat}\omega_{Ni}} \times 3600 \quad (3)$$

Where *J_{CO}* represents the local current density of CO, *M_{Ni}* represents the relative atomic mass of Ni, *n* represents the number of electron transfer in the product formation process (for CO and H₂, *n* = 2), *F* represents Faraday constant (96485 C/mol), *m_{cat}* represents the mass of the catalyst on the electrode, and *ω_{Ni}* represents the loading amount of Ni element in the catalyst.

2.4.3. Electrochemical measurements in flow cell

The flow cell reactor for CO₂RR consists of four polytetrafluoroethylene plates, three cavities of which include a gas chamber and two electrolyte chambers. An anion exchange membrane was used to separate the anode chamber from the cathode chamber. The carbon paper covered by 1 mg cm⁻² catalyst was used as gas diffusion layer (GDL) and working electrode (reaction area was 2×0.5 cm²). Hg/HgO electrode was placed in cathode chamber as reference electrode and the platinum sheet was used as the counter electrode. The 1 M KOH electrolyte was injected into the reactor at the rate of 20 mL min⁻¹ through a flow pump, and the high purity CO₂ gas was transported to the cathode chamber at the rate of 15.2 mL min⁻¹ through the mass flow controller.

During the test, all the test potentials can be converted based on the Nernst Eq. (4):

$$E \text{ (vs.RHE)} = E \text{ (vs.Hg/HgO)} + 0.098V + 0.0591 \times pH \quad (4)$$

All electrochemical tests and calculation methods are the same as those of the H-type cell mentioned above.

2.5. Computational methods

Density functional theory (DFT) calculations were carried out by using Vienna Ab initio Simulation Package (VASP).^[54,55] The generalized gradient approximation (GGA) within the Perdew-Burke-Ernzerhof (PBE) functional was adopted to describe the exchange correlation interaction.^[56] Projector augmented wave (PAW) method was applied with the cut-off energy of 450 eV.^[57] The D2 correction method by Grimme was used to illustrate the van der Waals interaction.^[58] The convergence criteria of energy and force were set to

1×10^{-5} eV and 0.02 eV \AA^{-1} , respectively. The Ag (200) surface was simulated with a 3×3 supercell, containing 4 layers. The NiAD@CN was simulated with a Ni_3N_6 site embedded in a 6×6 supercell of graphene. The NiAD/AgNPs@CN was modeled with a Ag_{13} cluster adsorbed on NiAD@CN.

3. Results and discussion

The synthetic procedure of NiAD/AgNPs@CN was illustrated in Fig. 1a by a carbon layer coating strategy. Firstly, a dark yellow precursor of $\text{Ag}/\text{g-C}_3\text{N}_4$ was obtained via pyrolysis of freeze-dried powder (including a certain amount of ammonium chloride, dicyandiamide, a certain proportion of nickel chloride and silver nitrate) at 550°C . In this process, dicyandiamide coordinates with Ag^+ and Ni^{2+} to form coordinative compounds, anchoring Ag, and Ni sites. With the decomposition of dicyandiamide, a large amount of NH_3 was released under high-temperature calcination, the Ag^+ , and Ni^{2+} were reduced to metal and then $\text{g-C}_3\text{N}_4$ was generated during pyrolysis. Secondly, a carbon layer coating strategy was adopted by the unitized 0.3 M glucose solution. A certain amount of powder was ultrasonically dispersed in 0.3 M glucose solution and hydrothermal at 180°C for 10 h. The hydrothermal sample was then calcined at 1000°C to form a CN matrix with good electrical conductivity. In the pyrolysis process, the glucose decomposes into small gas molecules and carbon layers, which avoids the complete decomposing of $\text{g-C}_3\text{N}_4$ and finally forms a rich-nitrogen-doped carbon substrate. This carbon coating method can stabilize atomically dispersed Ni and make it difficult to aggregate, thus

promoting the electrochemical kinetic reaction process.

Fig. 1b-i displays the morphology and microstructure of the NiAD/AgNPs@CN catalyst. As shown in Fig. 1b, the catalyst shows an amorphous flake structure. TEM image (Fig. 1c) reveals that a great number of nanoparticles with uniform particle sizes (~ 10 nm) are distributed on the ultrathin amorphous CN substrate. Partial amplification of the nanoparticles (Fig. 1d) shows obvious lattice stripes with a spacing of approximately 0.23 nm, corresponding to the (200) plane of Ag nanoparticles. According to the energy-dispersive X-ray spectroscopy (EDS) elemental mapping results (Fig. 1f-i), the catalyst contains four elements C, N, Ni, and Ag with uniform distribution, silver elements mainly exist in the form of nanoparticles while nickel elements are mainly dispersed on the CN substrate as atoms. Furthermore, aberration-corrected high-angle annular dark-field scanning transmission electron microscopy (AC-HAADF-STEM) images (Fig. 1j-l) were acquired to explain the microtopography. Ag nanoparticles and (200) plane were observed clearly in Fig. 1j-k, which agrees with TEM images. Notably, Ni atoms are scattered in Ni_n ($n = 2-4$) on the CN substrate, in which they are marked with red circles except for a very few single atoms, further unveiling that Ag NPs are surrounded by atomically dispersed nickel atoms (NiAD) on the CN substrate. For the convenience of comparison, SEM and TEM characterization were performed on the samples of the comparison groups (AgNPs@CN , NiAD@CN , NiNPs@CN , NiAD/AgNPs@CN-1 , NiAD/AgNPs@CN-2 , CN), as shown in the Figure S4-S9. Interestingly, it can be seen that through the similar synthesis process, Ag nanoparticles (~ 120 nm) and Ni atoms are generated on the CN substrate, respectively, when the silver source or nickel source is added

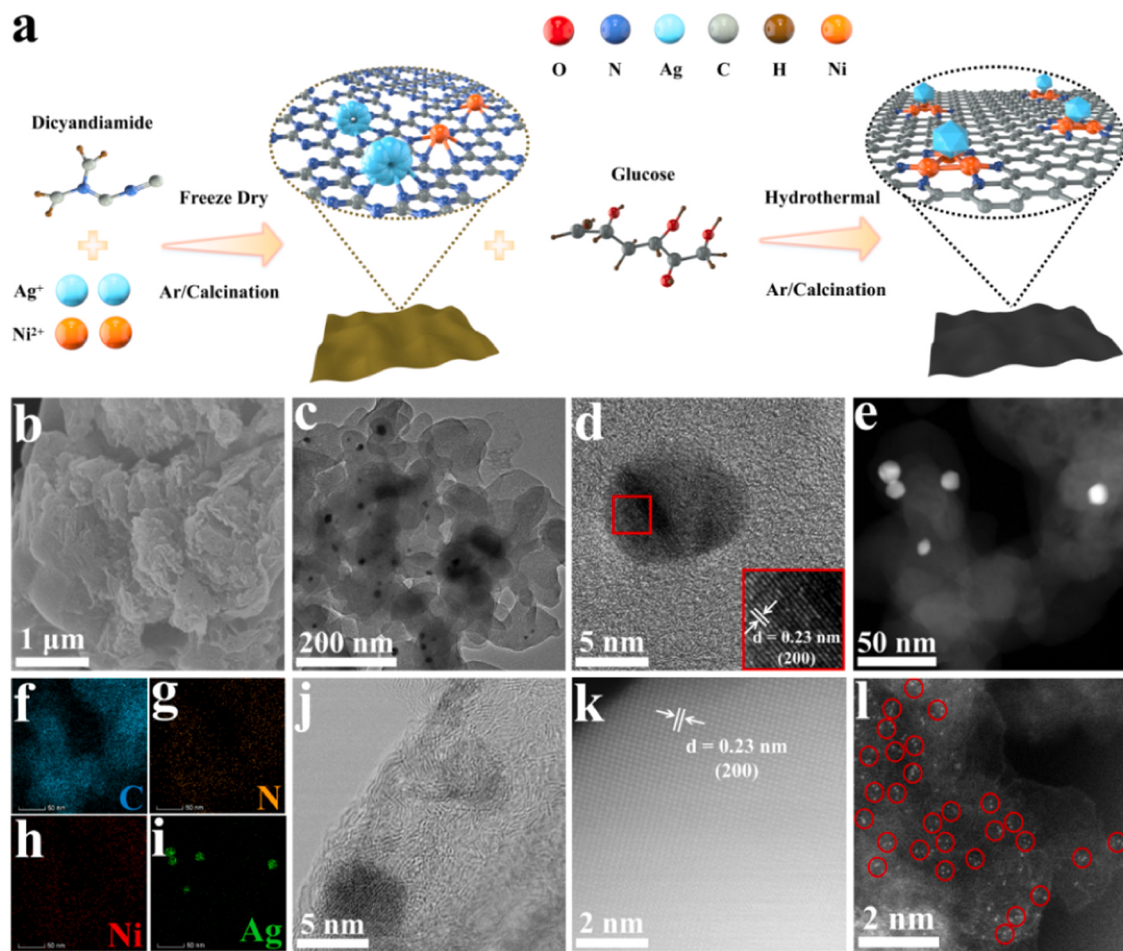


Fig. 1. (a) Scheme of the preparation process. (b) SEM image. (c) TEM image of the NiAD/AgNPs@CN sample. (d) HRTEM image of a single particle region of the NiAD/AgNPs@CN sample. (e), (f), (g), (h), and (i) STEM-EDX images of NiAD/AgNPs@CN sample with the corresponding C, N, Ag, and Ni elemental mappings. (j), and (l) AC-HAADF-STEM images of the NiAD/AgNPs@CN sample with the measured lattice fringe spacing. Nickel atoms are marked by red circles.

alone (Figure S4 and S5). Furthermore, if the nickel source is excessive, nickel particles (~ 30 nm) will be formed on the CN substrate, whereas silver element mainly tends to aggregate into nanoparticles. Although the proportion of silver in NiAD/AgNPs@CN-1 and NiAD/AgNPs@CN-2 is different from that in NiAD/AgNPs@CN, both of them also form a structure similar to NiAD/AgNPs@CN, which further indicates that when silver and nickel are present in the pyrolysis process, silver tends to aggregate, while nickel is indeed dispersed into atoms. (Figures S7 and S8).

XRD patterns of the catalysts were obtained for structural analysis (Fig. 2a and Figure S10a). As shown in Fig. 2a, it can be observed four characteristic diffraction peaks at 38.1° , 44.3° , 64.2° , and 77.5° in the catalysts AgNPs@CN and NiAD/AgNPs@CN, which correspond to the (111), (200), (220) and (311) crystal planes of silver nanoparticles, respectively. It is worth noting that the peaks of silver in NiAD/AgNPs@CN is significantly weaker than that of AgNPs@CN, mainly due to the smaller size of silver nanoparticles in NiAD/AgNPs@CN formed by the protection of the carbon layer strategy. Moreover, the intensity of the four characteristic diffraction peaks increases significantly with the increase of silver content in the catalysts with different Ag/Ni mole ratios (Figure S10a). At the same time, no characteristic diffraction peaks of nickel particles at 44.5° and 51.8° are observed in the silver-containing samples, implying that nickel element exists in the form of atomic level dispersed, which agrees with the results of AC-HAADF-STEM images. There is no obvious characteristic diffraction peak of nickel in NiAD@CN material which further indicates that nickel is dispersed in the form of atoms.

To further understand the electronic structure of the synthesized materials, the element composition and chemical valence were measured by X-ray photoelectron spectroscopy (XPS). XPS survey spectra for the catalysts were obtained in Figure S11. For the high-resolution Ag 3d spectra of four silver-doped samples (NiAD/AgNPs@CN, NiAD/AgNPs@CN-1, NiAD/AgNPs@CN-2 and AgNPs@CN), the binding energies of Ag 3d_{5/2} is 368.3 eV (Fig. 2b and Figure S10b), corresponding to the zero valence of silver element, indicating that Ag element mainly exists in the form of metal valence

state in these four samples. [59] This is consistent with the results of XRD and TEM. From the high-resolution Ni 2p spectra of Nickle-doped samples (NiAD/AgNPs@CN, NiAD@CN and NiNPs@CN, Fig. 2c), the binding energy of Ni 2p_{3/2} is about 855.0 eV in NiAD/AgNPs@CN and NiAD@CN, which is higher than the reported Ni⁰ (≈ 853.0 eV) and lower than the Ni²⁺ (≈ 855.7 eV), indicating that nickel exists in the form of intermediate valence between Ni⁰ and Ni²⁺. [60,61] For NiNPs@CN catalyst, the binding energy of Ni 2p_{3/2} should appear around 853.0 eV in theory, but it shifts to 855.25 eV. This may be due to surface oxidation caused by the high sensitivity of Ni nanoparticles to air as well as the limitation of X-ray penetration, which makes the zero valence state of Ni nanoparticles in the composition difficult to detect and finally exists in a high valence state. As shown in Fig. 2d, the high-resolution N 1 s spectra of NiAD/AgNPs@CN, CN, and NiAD@CN show three kinds of nitrogen which are ascribed to pyridinic-N (398.4 eV), graphitic-N (401.2 eV) and nitrogen oxide (N-O) (403.4 eV). [62,63] Pyridinic-N is considered to be the main source of coordination with transition metal species due to the existence of π orbital lone pair electrons. [64,65] It is worth noting that the proportion of pyridinic-N in NiAD/AgNPs@CN and NiAD@CN is 25.92% and 18.74%, respectively, which is much higher than that of CN (15.21%) and other silver-containing catalysts (NiAD/AgNPs@CN-1, NiAD/AgNPs@CN-2, AgNPs@CN) (Figure S12), demonstrating that the maximum Ni-Nx coordination in NiAD/AgNPs@CN. Furthermore, the Raman spectrum (Figure S13 and S14) displays that the maximum value of I_D/I_G is 1.56 of NiAD/AgNPs@CN catalyst, revealing that with the increase of pyridinic-N, the number of Nickel atoms that can participate in coordination also increases, resulting in the reduction of graphitization degree of materials. These results further explain that nickel element in NiAD/AgNPs@CN exists in the form of atomic dispersed, which is consistent with the XRD and AC-HAADF-STEM analysis.

To further study the electronic structure and coordination environment of the materials, Ni K-edge X-ray absorption near-edge structure (XANES) spectra and the extended X-ray absorption fine structure (EXAFS) spectra were used to analyze NiAD/AgNPs@CN and NiAD@CN catalysts. The Ni K-edge XANES spectrum is displayed in Fig. 3a. Ni foil (Ni⁰) and Ni(OH)₂ (Ni²⁺) are traditional contrast samples, while Ni

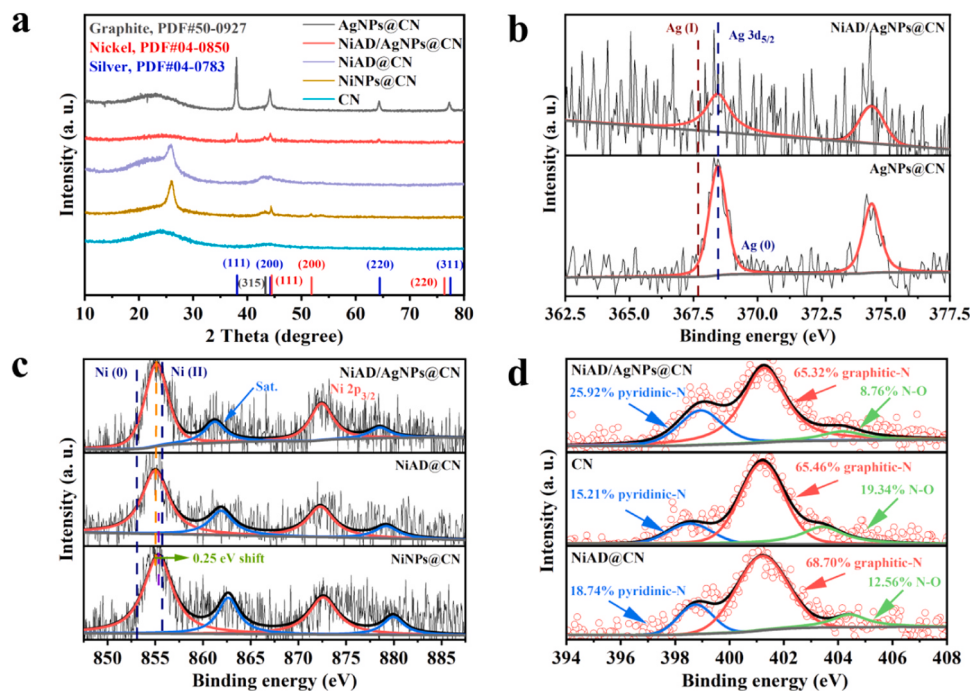


Fig. 2. (a) XRD pattern of NiAD/AgNPs@CN and the other four reference samples. XPS of (b) High-resolution Ag 3d spectra for NiAD/AgNPs@CN and AgNPs@CN samples; (c) High-resolution Ni 2p spectra for NiAD/AgNPs@CN, NiAD@CN and NiNPs@CN samples; (d) High-resolution N 1 s spectra for NiAD/AgNPs@CN, CN, and NiAD@CN samples.

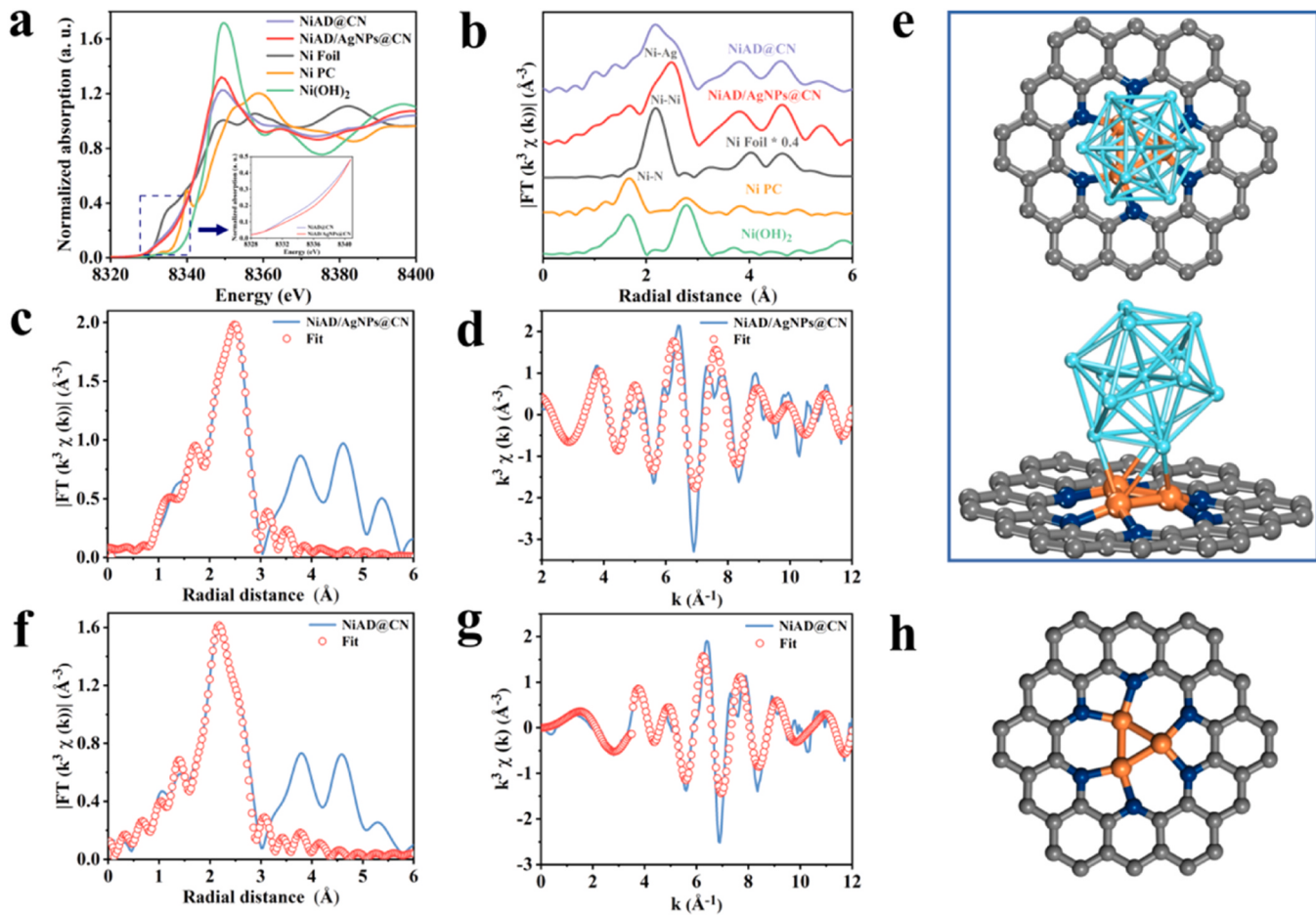


Fig. 3. (a) Normalized Ni K-edge XANES spectra of five samples. (b) Fourier transform EXAFS spectra for the Ni K-edge of NiAD/AgNPs@CN and related samples in R space. (c) R space experimental data and fitting curve of NiAD/AgNPs@CN sample. (d) K space experimental data and fitting curve of NiAD/AgNPs@CN sample. (e) The calculated model of NiAD/AgNPs@CN sample (Ag in cyan, Ni in orange, N in blue, and C in grey). (f) R space experimental data and fitting curve of NiAD@CN sample. (g) K space experimental data and fitting curve of NiAD@CN sample. (h) The calculated model of NiAD@CN sample (Ni in orange, N in blue, and C in grey).

phthalocyanine material (Ni PC) with a good Ni-N₄ coordination structure is also selected as a reference sample. The pre-edge curve of Ni species in NiAD/AgNPs@CN and NiAD@CN catalysts is between Ni foil and Ni(OH)₂, indicating that the Ni species in both catalysts are partially oxidized state with an intermediate valence state ($\text{Ni}^0 < \text{Ni}^{\delta+} < \text{Ni}^{2+}$) close to Ni^{1+} . More importantly, the valence state of the Ni atom in NiAD/AgNPs@CN is slightly higher than that of NiAD@CN, suggesting that the binding energy of Ni species slightly rises due to the addition of silver, which corresponds to the height of the white-line peak. As shown in Fig. 3b, compared with the reference samples, the Fourier transform (FT) k^3 -weighted $\chi(k)$ function of the EXAFS spectra shows that catalyst NiAD@CN exhibits a shoulder peak at 1.7 Å and another peak 2.1 Å, which can belong to the Ni-N and Ni-Ni coordination, respectively. While, as for NiAD/AgNPs@CN catalyst, except for the similar FT peak positions (1.7 Å, 2.1 Å) with NiAD@CN, there is also a main strong peak at 2.6 Å, which can be indexed to the Ni-Ag coordination. It's worth noting that the FT peak intensity of Ni-Ni shows a shoulder peak that is also different from NiAD@CN, indicating that the involvement of silver causes most nickel species to interact with silver. That means nickel atoms can not only coordinate with N atoms but also have an electronic interaction with silver. By fitting the first nearest shell of R space $1.0 \leq R$ (Å) ≤ 3.3 , the local structure of NiAD/AgNPs@CN and NiAD@CN was obtained, respectively, as shown in Fig. 3c-g, the Ni-N coordination number is 2 and the Ni-Ni coordination number is 2, which is different from Ni foil (Figure S15). Furthermore, based on AC-HAADF-STEM, density functional theory (DFT) was used to further deduce the

possible structure of the two catalysts. The calculated models are shown in Figs. 3e-3h, the $\chi(k)$ function of the EXAFS spectra generated based on this model (Fig. 3c and f) fit well with the experimental spectra. Especially, to show the structure clearly, the model of NiAD/AgNPs@CN from two different perspectives was presented in Fig. 3e. The results demonstrate that the Ni atoms in NiAD/AgNPs@CN are atomically dispersed in the form of Ni trimer (Ni_3) without forming Ni clusters or nanoparticles. The Ni_3 is embedded in the C-N ring and coordinated with Ag. Therefore, based on the above discussion, the dominant active sites for NiAD/AgNPs@CN can be speculated as Ag sides and atomically dispersed Ni_3 sides on the CN substrate.

For the sake of exploring the internal structure-activity relationship of the materials, the electrochemical tests were conducted in a H-type electrolytic cell filled with 0.1 M CO_2 -saturated KHCO_3 solution. The linear sweep voltammetry (LSV) results were obtained as shown in Fig. 4a. With the negative shift of potential, the current density increases in varying degrees on the catalysts. The maximum current density values were observed at -1.38 V (vs. RHE) obviously, the CN catalyst reaches the lowest current density ($\sim 9.5 \text{ mA cm}^{-2}$), indicating that the bare CN matrix displays poor reactive activity. With the involvement of Ag or Ni metal active sites, the current density of several materials is higher than that of CN substrate. In particular, the AgNPs@CN catalyst shows the highest current density ($\sim 19.5 \text{ mA cm}^{-2}$) due to its best conductivity. The current density of NiNPs@CN catalyst is only 4 mA cm^{-2} . However, when Ni is coordinated with N and atomically dispersed on CN substrate, as for the NiAD@CN sample, the current density increases

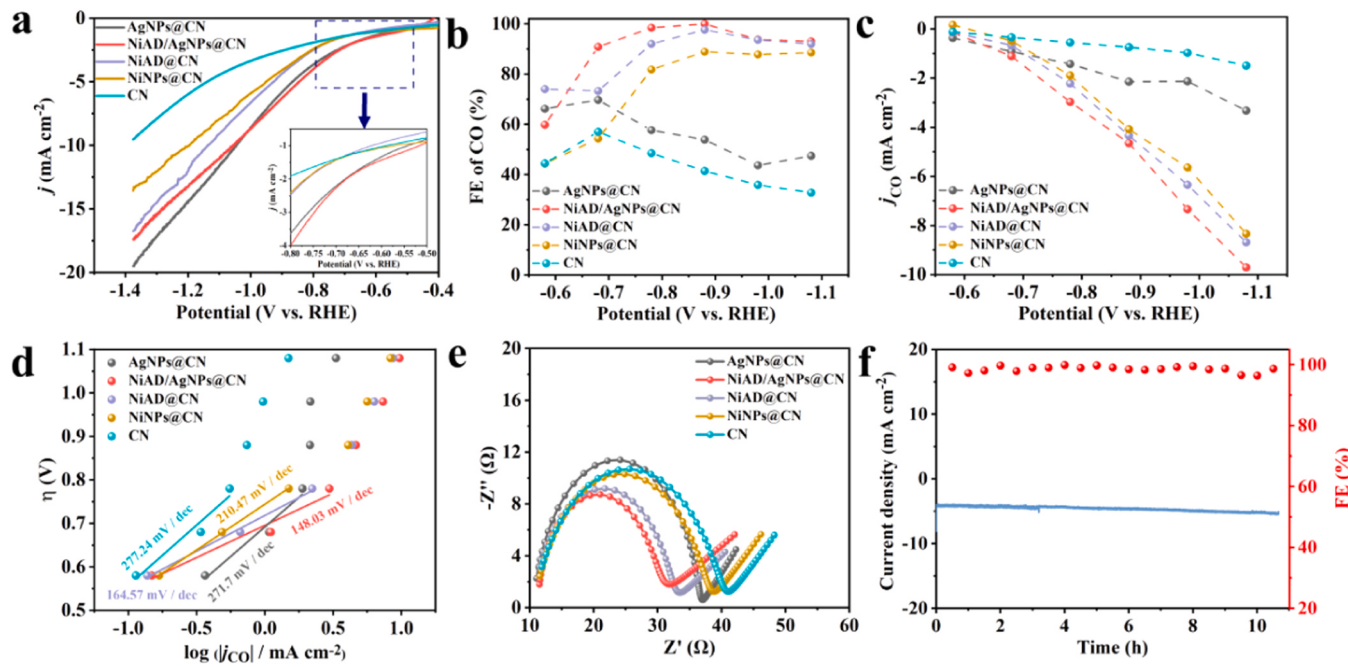


Fig. 4. (a) The LSV curves, (b) CO Faradaic efficiency, (c) CO partial current density, (d) Tafel plots obtained in 0.1 M CO_2 -saturated KHCO_3 electrolyte, and (e) Nyquist plots of five samples. (f) Long-time electrolysis experiment of NiAD/AgNPs@CN at -0.88 V vs. RHE for 10.5 h.

significantly with the maximum ~ 16.8 mA cm $^{-2}$. NiAD/AgNPs@CN exhibits a higher current density (~ 17.4 mA cm $^{-2}$) due to the unique structure of Ni_3 atomically dispersed around Ag NPs. Besides, the NiAD/AgNPs@CN sample preferentially exhibits the highest current density at a lower potential range of -0.5 V to -0.8 V (vs. RHE). This implies that NiAD/AgNPs@CN catalyst has a lower reaction overpotential and faster kinetics in CO_2 RR. On the contrary, in Ar-saturated 0.1 M KHCO_3 solution, NiAD/AgNPs@CN shows lower current density (~ 9.5 mA cm $^{-2}$), which indicates that the good catalytic activity comes from the CO_2 reduction reaction (Figure S16). Furthermore, compared with NiAD/AgNPs@CN and AgNPs@CN catalysts, the lowest current density of NiAD/AgNPs@CN in the whole potential range suggesting that the synergism between Ag NPs and Ni_3 in the reaction process can well inhibit the occurrence of HER side reaction. (Figure S17).

Then, in order to quantify the selectivity of materials in the CO_2 reduction reaction, the Faraday efficiency of several materials was analyzed according to I-T curves at different potentials (Fig. 4b). For all the catalysts, only CO and H_2 were found in the gas phase products, and no characteristic peak of liquid phase products was observed in ^1H NMR (Figure S18a). As shown in Fig. 4b, the CN material shows a lower FE_{CO} than the other catalysts, in which the FE_{CO} reaches the maximum of only 57.03% at -0.68 V (vs. RHE). The FE_{CO} of the AgNPs@CN sample is higher than that of CN, reaching 66.17% at -0.58 V (vs. RHE). The maximum FE_{CO} is 69.71%, which is due to the favorable adsorption of CO_2 by Ag nanoparticles. However, when the potential continues to be negative, FE_{CO} begins to decrease, implying that the hydrogen evolution reaction (HER) begins to participate in the competition, and the HER reaction is dominant at high potential (Figure S18b). On the other hand, NiAD@CN shows good catalytic activity in the whole potential range because of the maximum utilization of atoms and the active sites exposed on the surface. When the potential is between -0.78 V \sim -1.08 V (vs. RHE), the FE_{CO} is more than 85%, and the maximum FE_{CO} reaches 97.65% at -0.88 V (vs. RHE). More importantly, due to the synergy between Ag-Ni, NiAD/AgNPs@CN exhibits superior performance which surpasses that of the other contrast catalysts. As shown in Fig. 4b, the FE_{CO} of NiAD/AgNPs@CN catalyst shows up to 90.84% at -0.68 V (vs. RHE), which is approximately 1.3 times that of NiAD@CN and AgNPs@CN catalysts. Furthermore, in the wide potential range of

-0.68 V \sim -1.08 V (vs. RHE), the FE_{CO} of NiAD/AgNPs@CN catalyst is higher than 90%, and the maximum FE_{CO} reaches nearly 100% at -0.88 V (vs. RHE). This result further manifests that the synergism between Ag NPs and Ni_3 in the reaction process makes the side reaction HER well suppressed.

The local current density j_{CO} diagram of CO under different applied potentials is obtained based on j_{total} and FE_{CO}. As shown in Fig. 4c, the j_{CO} of NiAD/AgNPs@CN is higher than that of other catalysts in the potential range of -0.68 V \sim -1.08 V (vs. RHE). Particularly at the potential of -1.08 V (vs. RHE), the j_{CO} reaches 9.07 mA cm $^{-2}$, which is 3 times that of AgNPs@CN and 1.1 times that of NiAD@CN, respectively. To evaluate the real reaction activity, the electrochemical active surface area (ECSA) was acquired by calculating the double-layer capacitance (C_{dl}) (Figure S19 and S20a). The normalized current density of ECSA is obtained as shown in Figure S20b. As shown in the Figure S20b, the current density of NiAD/AgNPs@CN is the highest in a wide potential range of -0.68 V \sim -1.08 V (vs. RHE). At -1.08 V, the current density of NiAD/AgNPs@CN catalyst is 1.05 times that of NiAD@CN and 3.41 times that of AgNPs@CN, respectively.

In addition, the reaction kinetics of different materials in the process of CO_2 reduction were studied by Tafel slopes as shown in Fig. 4d. Compared with other catalysts, NiAD/AgNPs@CN has the smallest Tafel slope (148 mV dec $^{-1}$), suggesting that it has the fastest reaction kinetics in the process of CO_2 reduction to CO. And the value is close to that of 118 mV dec $^{-1}$, implying that the single electron transfer step of CO_2 adsorption is the rate-determining step.[66,67] Furthermore, through the electrochemical impedance test (Fig. 4e), NiAD/AgNPs@CN shows the smallest semicircle diameter, suggesting that the catalyst has the fastest charge transfer rate in the process of CO_2 reduction. This is consistent with the results of Tafel slopes.

Stability is an important index to evaluate whether the catalyst has the potential for industrial application. Considering the current density and FE_{CO}, the stability of NiAD/AgNPs@CN catalyst was tested under -0.88 V (vs. RHE) potential (Fig. 4f). After the 10.5 h test, the FE_{CO} of the catalyst remained above 95%, and the current density had no obvious attenuation, showing excellent stability. Through the SEM and TEM characterization of the reacted sample (Figure S21), we found that the structure of the sample did not change obviously, and there were still

uniform silver nanoparticles loaded on the surface of the amorphous CN carrier. As shown in Figure S21c, obvious lattice stripes corresponding to the (200) plane of silver nanoparticles can be observed which further proves good stability.

In view of the slow mass transfer rate of CO_2 molecules in aqueous solution, the catalyst usually shows low current density when reacting in H-type cell. However, the flow cell reactor is a potential electrochemical reaction device with industrial application prospects, which can overcome mass transfer problems. For this reason, we carried out CO_2RR in a flow cell filled with 1 M CO_2 -saturated KOH electrolyte, in order to obtain higher current density and faster reaction kinetics. As shown in Figure S22a, the LSV curve shows that the current density of NiAD/AgNPs@CN catalyst in the flow cell is higher than that of the H-type cell, especially at -1.25 V (vs. RHE), the current density is 178.2 mA cm^{-2} , which is much higher than 14.3 mA cm^{-2} at the corresponding potential in the H-type cell (Fig. 4a). In addition, the catalyst shows a lower initial reaction potential (-0.25 V (vs. RHE)) in the flow cell showing that the flow cell reactor can eliminate the kinetic resistance to some extent and can effectively promote the mass transfer efficiency of CO_2 molecules in aqueous solution, thus significantly increasing the current density and catalytic activity. Then, as shown in Figure S22b, in the flow cell, NiAD/AgNPs@CN catalyst can still show a good conversion from CO_2 to CO in a wide potential range of -0.68 V \sim -1.08 V (vs. RHE), and at -0.88 V (vs. RHE), the FE_{CO} reaches the maximum value ($> 90\%$) with a high current density of 79.70 mA cm^{-2} . In addition, with the increase of applied potential, the j_{total} and j_{CO} of NiAD/AgNPs@CN catalyst will also increase. At -1.08 V (vs. RHE), the j_{total} of 109.1 mA cm^{-2} and the j_{CO} of 78.04 mA cm^{-2} can be recorded, further proving that the catalyst has good application prospects.

To further clarify the mechanistic insights on NiAD/AgNPs@CN catalyst, and reveal the true reaction sites and path, the influence of Ni-Ni coordination and Ag clusters on the atomic level was investigated by DFT calculation. Based on the experimental results, three models (NiAD@CN, NiAD/AgNPs@CN, Ag (200)) were established as shown in Fig. 5a. Ag (200) was used as the targeted structure for Ag nanoparticles, as per the AC-HAADF-STEM results (Fig. 1d and k). The reaction path of CO_2RR usually includes the following processes. Firstly, CO_2 is adsorbed on the active site of the catalyst surface. Secondly, under the activation of the active site, the CO_2 molecule reacts with the proton-electron in the solution to form the reaction intermediate $^{*}\text{COOH}$. Thirdly, $^{*}\text{COOH}$ is further coupled with proton-electron to generate $^{*}\text{CO}$ and water

molecules. Finally, $^{*}\text{CO}$ desorption, the active sites are exposed again and continue to react. Since there are two possible active parts (Ni₃ and Ag clusters) in the structure of NiAD/AgNPs@CN, to explore the real reaction sites at the interface, all of the possible reaction sites for CO_2 adsorption were constructed for the DFT study. As shown in Figure S23, the most possible three initial adsorption sites are: i CO_2 molecules adsorbed on the side of Ni₃, ii CO_2 molecules adsorbed on the Ag cluster side, and iii CO_2 molecules are adsorbed on the interface formed by Ni₃ and Ag cluster. It is worth noting that in order to reduce computational complexity, we use Ag₁₃ clusters instead of Ag nanoparticles in the model. For this reason, we only consider the Ag adsorption sites in contact with Ni to study the synergistic effect of Ni-Ag. The other sites on the Ag₁₃ cluster do not exist in the real material, so the other adsorption sites will not be considered too much. For comparison, the schematic atomic structure of CO_2RR on NiAD@CN, and Ag (200) sites were also given out (Figure S24). Subsequently, the studies of CO_2RR activities of the three samples were performed and Gibbs free energies were calculated as shown in Fig. 5b. Atomic-scale dispersed NiAD@CN shows the lowest free energy of -0.53 eV when generating reaction intermediate $^{*}\text{COOH}$ by proton-electron coupling, indicating Ni₃ has the strongest effect with CO_2 molecules. Meanwhile, the $^{*}\text{CO}$ desorption process shows the highest energy barrier. It means that $^{*}\text{CO} \rightarrow \text{CO} + *$ is the rate-determining step in the CO_2RR for NiAD@CN, and the high energy barrier will limit the catalytic activity for the conversion of CO_2 to CO.

On the contrary, Ag (200) shows the highest Gibbs free energy of $^{*}\text{COOH}$ formation (0.95 eV) and the lowest free energy of $^{*}\text{CO}$ desorption (0.08 eV), demonstrating the rate-determining step in the CO_2RR for the AgNPs@CN is $^{*}\text{COOH}$ formation since of the weak activation of Ag (200) on CO_2 . Owing to the large energy barrier of $^{*}\text{COOH}$ generation, the catalytic activity of the catalyst AgNPs@CN during the CO_2RR reaction is poor. This is consistent with the experimental results.

As for NiAD/AgNPs@CN, the lowest free energy of $^{*}\text{COOH}$ formation appeared on the sites ii. (CO_2 is adsorbed on the Ag side), which is 0.45 eV, much lower than 0.95 eV of the Ag (200) crystal surface. That means under the regulation of Ni₃, the activation of CO_2 on the Ag cluster is significantly enhanced, thus reducing the reaction energy barrier of the $^{*}\text{COOH}$ formation, making the first proton-electron coupling process easier to occur. Meanwhile, the lowest $^{*}\text{CO}$ desorption energy barrier (0.36 eV) also appeared on site ii, which is significantly lower than that of $^{*}\text{CO}$ desorption on Ni₃ (2.95 eV) (details see Table S2). Obviously, the interaction between Ag and Ni₃ significantly

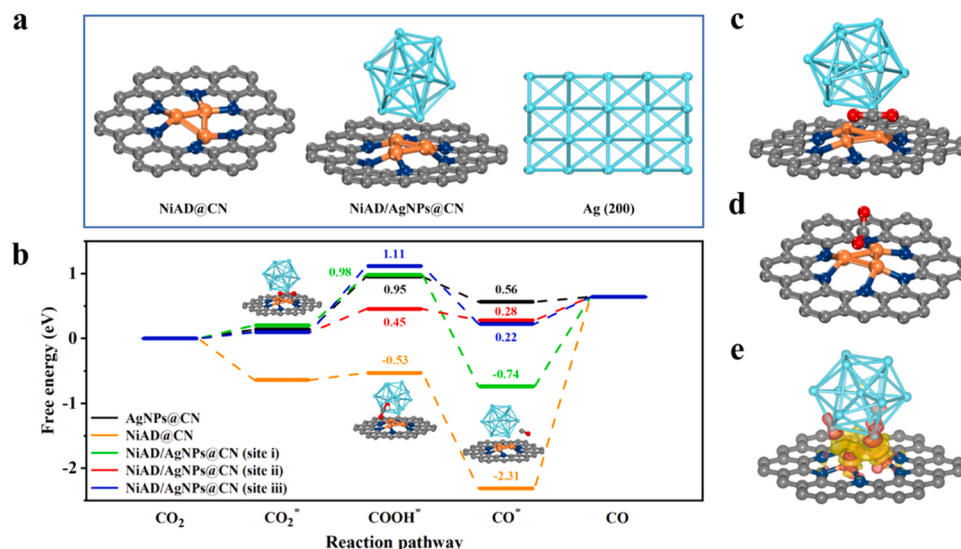


Fig. 5. (a) Optimized atomic structures including NiAD@CN, NiAD/AgNPs@CN, and Ag (200) (C, N, and Ni atoms are represented by gray, blue, and orange, respectively). (b) DFT calculated free energy profiles for CO_2RR . (c) and (d) Optimized structures of NiAD/AgNPs@CN and NiAD@CN with adsorbed CO_2 . (e) The optimized structure and the view of charge density difference of NiAD/AgNPs@CN.

reduces the energy barrier of $^*\text{CO}$ desorption, which is more conducive to the exposure of active sites and the occurrence of subsequent reactions. In comparison, the calculation of site i and iii shows that the free energy of generating $^*\text{COOH}$ is 0.98 and 1.11 eV respectively, even higher than that of the Ag (200) surface. Combined with the experimental results, this shows that site ii (adsorption on the Ag side) is more reasonable, and the real reaction site is on the Ag side. In addition, we also found an interesting phenomenon in the calculation process. When the initial adsorption site of CO_2 is at the interface, CO_2 molecules will spontaneously far away from the Ni atom and approach to Ag atom, and finally generate the same configuration as CO_2 adsorbed on Ag sites, which further suggests that under the regulation of Ni_3 , the adsorption effect of Ag on CO_2 is significantly enhanced.

To prove the above conclusion, the adsorption energy of CO_2 molecules was further calculated for Ag (200), Ni_3 , and three reaction sites of NiAD/AgNPs@CN. The values of site ii and site iii coincide because CO_2 molecules spontaneously move to the Ag side during dynamic optimization (Fig. 5c). As shown in Figure S25, when the CO_2 molecule adsorbed on Ni_3 , the original linear CO_2 molecule bends (Fig. 5d), and the adsorption energy of Ni_3 for CO_2 is -1.14 eV, indicating a strong activation of Ni_3 for CO_2 . In comparison, the adsorption energy of CO_2 on Ag (200) is only -0.24 eV. When Ni_3 and Ag cluster are combined, the adsorption energy of CO_2 is significantly increased to -0.34 eV. This conclusion indicates the internal reason for the successful regulation of NiAD/AgNPs@CN active site.

The differential charge density is further calculated for NiAD/AgNPs@CN to discuss the nature reason of the difference in catalytic activity as shown in Fig. 5e. The electronic structure of Ni^0 is $3d^8$, it is relatively stable due to the half full occupation of e_g orbits. While, in the coordination environment, the calculated spin value of Ni in NiAD is about 1.0 indicating Ni present as Ni^{1+} . Under this condition, the e_g orbit is occupied by only one electron, which is unstable and tend to transfer to CO_2 molecule. Therefore, Ni_3 structure in NiAD has a strong activation effect on CO_2 , however, when Ag cluster and Ni_3 contact, the three Ni atoms originally embedded in the CN ring are pulled out of the ring plane by Ag atoms. At the same time, partial electrons of Ag transfer to Ni_3 , resulting in the decrease of the spin number of Ni from 1 to 0.4, which is also consistent with the results of XANES. After the spin electron orbit of Ni receives some electrons, the energy level of Ni e_g orbit changes, resulting in difficulty transferring of electron from Ni to CO_2 . It is consistent with the conclusion that the adsorption strength of CO_2 on Ni_3 sites decreased significantly after recombination with Ag cluster.

On the contrary, after Ag loses part of its electrons, the electrons of 4d orbits become unstable, making it easier to transfer from Ag to CO_2 molecules, thus strengthening the activation of Ag to CO_2 molecules. Therefore, the change of the spin orbital energy level caused by the electron transfer between Ag cluster and Ni_3 is the essential reason for the change of their respective CO_2 activation.

Furthermore, we calculated the partial density of states (PDOS) of the Ag site and Ni site in three comparison materials (NiAD@CN, AgNPs@CN, NiAD/AgNPs@CN), which can directly reflect the activity of the sites (Figure S26). The D-bend centre of the Ni_3 site shifts to lower energy far away from the Fermi energy level indicating that adsorption energy on these sites weakens. In contrast, compared to PDOS of Ag in Ag particles, the D-bend centre of Ag sites in NiAD/AgNPs@CN shift to Fermi energy level indicating that the strengthening of reaction intermediates at Ag sites, which reduces the activation energy of the reaction, thereby accelerating the reaction. These results are consistent with the DFT results.

4. Conclusion

In summary, we have designed a highly effective electrocatalyst NiAD/AgNPs@CN with a complex structure of atomic-level dispersed Ni_3 active center surrounding Ag nanoparticles by carbon layer coating strategy in this work. The unique structure makes the catalyst NiAD/

AgNPs@CN show a good CO_2RR performance at a moderate potential -0.88 V (vs. RHE) with a FE_{CO} of nearly 100% in H-type cell and a high current density of 79.70 mA/cm² with a $\text{FE}_{\text{CO}} \sim 91.77\%$ in the flow cell. DFT calculation reveals that the atomically dispersed nickel active sites can effectively improve the activation of CO_2 on silver nanoparticles, by modulating the spin electronic state which can reduce energy consumption and improve the activity of CO_2RR . This work reveals the true active sites and synergistic catalytic mechanisms in complex materials and provides a new idea for the design of efficient catalysts.

Credit authorship contribution statement

The manuscript was written through contributions of all authors. All authors have given approval to the final version of the manuscript.

CRedit authorship contribution statement

Jun Chen: Writing – review & editing, Supervision. **Yajuan Wei:** Writing – review & editing, Funding acquisition, Formal analysis, Data curation, Conceptualization. **Jingbo Zhang:** Writing – review & editing, Supervision, Funding acquisition. **Liu Lin:** Investigation, Data curation. **Zibo Zhao:** Writing – original draft, Investigation, Data curation. **Lanlan Feng:** Data curation. **Yuwen Wang:** Data curation. **Youxuan Ni:** Methodology, Data curation. **Lin Jin:** Data curation.

Declaration of Competing Interest

The authors declare that they have no known competing financial interests or personal relationships that could have appeared to influence the work reported in this paper.

Data Availability

Data will be made available on request.

Acknowledgments

This work was financially supported by the National Natural Science Foundation of China (Grant Nos. 51801105 and 21975183), Doctoral research project of Tianjin Normal University (Grant No. 52XB2105).

We are also grateful to Professor Jia Liu of Tianjin University for his guidance and help in theoretical calculation.

Appendix A. Supporting information

Supplementary data associated with this article can be found in the online version at [doi:10.1016/j.apcatb.2024.123886](https://doi.org/10.1016/j.apcatb.2024.123886).

References

- [1] H. Yang, Q. Lin, C. Zhang, X. Yu, Z. Cheng, G. Li, Q. Hu, X. Ren, Q. Zhang, J. Liu, C. He, Carbon dioxide electroreduction on single-atom nickel decorated carbon membranes with industry compatible current densities, *Nat. Commun.* 11 (2020) 593, <https://doi.org/10.1038/s41467-020-14402-0>.
- [2] J. Feng, H. Gao, L. Zheng, Z. Chen, S. Zeng, C. Jiang, H. Dong, L. Liu, S. Zhang, X. Zhang, A $\text{Mn}-\text{N}_3$ single-atom catalyst embedded in graphitic carbon nitride for efficient CO_2 electroreduction, *Nat. Commun.* 11 (2020) 4341, <https://doi.org/10.1038/s41467-020-18143-y>.
- [3] K. Wang, D. Liu, L. Liu, J. Liu, X. Hu, P. Li, M. Li, A.S. Vasenko, C. Xiao, S. Ding, Tuning the local electronic structure of oxygen vacancies over copper-doped zinc oxide for efficient CO_2 electroreduction, *eScience* 2 (2022) 518–528, <https://doi.org/10.1016/j.esci.2022.08.002>.
- [4] E. Zhang, T. Wang, K. Yu, J. Liu, W. Chen, A. Li, H. Rong, R. Lin, S. Ji, X. Zheng, Y. Wang, L. Zheng, C. Chen, D. Wang, J. Zhang, Y. Li, Bismuth single atoms resulting from transformation of metal-organic frameworks and their use as electrocatalysts for CO_2 reduction, *J. Am. Chem. Soc.* 141 (2019) 16569–16573, <https://doi.org/10.1021/jacs.9b08259>.
- [5] Y. Zhou, A.J. Martín, F. Dattila, S. Xi, N. López, J. Pérez-Ramírez, B.S. Yeo, Long-chain hydrocarbons by CO_2 electroreduction using polarized nickel catalysts, *Nat. Catal.* 5 (2022) 545–554, <https://doi.org/10.1038/s41929-022-00803-5>.

[6] H. Li, K. Gan, R. Li, H. Huang, J. Niu, Z. Chen, J. Zhou, Y. Yu, J. Qiu, X. He, Highly dispersed NiO clusters induced electron delocalization of Ni-N-C catalysts for enhanced CO₂ electroreduction, *Adv. Funct. Mater.* 33 (2023) 2208622, <https://doi.org/10.1002/adfm.202208622>.

[7] Y. Chen, Z. Fan, J. Wang, C. Ling, W. Niu, Z. Huang, G. Liu, B. Chen, Z. Lai, X. Liu, B. Li, Y. Zong, L. Gu, J. Wang, X. Wang, H. Zhang, Ethylene selectivity in electrocatalytic CO₂ reduction on Cu nanomaterials: a crystal phase-dependent study, *J. Am. Chem. Soc.* 142 (2020) 12760–12766, <https://doi.org/10.1021/jacs.0c04981>.

[8] N. Zhang, X. Zhang, L. Tao, P. Jiang, C. Ye, R. Lin, Z. Huang, A. Li, D. Pang, H. Yan, Y. Wang, P. Xu, S. An, Q. Zhang, L. Liu, S. Du, X. Han, D. Wang, Y. Li, Silver single-atom catalyst for efficient electrochemical CO₂ reduction synthesized from thermal transformation and surface reconstruction, *Angew. Chem. Int. Ed.* 60 (2021) 6170–6176, <https://doi.org/10.1002/anie.202014718>.

[9] Y. Ma, J. Wang, J. Yu, J. Zhou, X. Zhou, H. Li, Z. He, H. Long, Y. Wang, P. Lu, J. Yin, H. Sun, Z. Zhang, Z. Fan, Surface modification of metal materials for high-performance electrocatalytic carbon dioxide reduction, *Matter* 4 (2021) 888–926, <https://doi.org/10.1016/j.matt.2021.01.007>.

[10] X. Zhang, J. Li, Y.-Y. Li, Y. Jung, Y. Kuang, G. Zhu, Y. Liang, H. Dai, Selective and high current CO₂ electro-reduction to multicarbon products in near-neutral KCl electrolytes, *J. Am. Chem. Soc.* 143 (2021) 3245–3255, <https://doi.org/10.1021/jacs.0c13427>.

[11] Y. Ma, J. Yu, M. Sun, B. Chen, X. Zhou, C. Ye, Z. Guan, W. Guo, G. Wang, S. Lu, D. Xia, Y. Wang, Z. He, L. Zheng, Q. Yun, L. Wang, J. Zhou, P. Lu, J. Yin, Y. Zhao, Z. Luo, L. Zhai, L. Liao, Z. Zhu, R. Ye, Y. Chen, Y. Lu, S. Xi, B. Huang, C.-S. Lee, Z. Fan, Confined growth of silver-copper janus nanostructures with {100} facets for highly selective tandem electrocatalytic carbon dioxide reduction, *Adv. Mater.* 34 (2022) 2110607, <https://doi.org/10.1002/adma.202110607>.

[12] S. Gong, W. Wang, R. Lu, M. Zhu, H. Wang, Y. Zhang, J. Xie, C. Wu, J. Liu, M. Li, S. Shao, G. Zhu, X. Lv, Mediating heterogenized nickel phthalocyanine into isolated Ni-N₃ moiety for improving activity and stability of electrocatalytic CO₂ reduction, *Appl. Catal. B* 318 (2022) 121813, <https://doi.org/10.1016/j.apcatb.2022.121813>.

[13] J. Han, N. Wang, X. Li, H. Lei, Y. Wang, H. Guo, X. Jin, Q. Zhang, X. Peng, X.-P. Zhang, W. Zhang, U.-P. Apfel, R. Cao, Bioinspired iron porphyrins with appended poly-pyridine/amine units for boosted electrocatalytic CO₂ reduction reaction, *eScience* 2 (2022) 623–631, <https://doi.org/10.1016/j.esci.2022.06.003>.

[14] J. d Yi, X. Gao, H. Zhou, W. Chen, Y. Wu, Design of Co-Cu diatomic site catalysts for high-efficiency synergistic CO₂ electroreduction at industrial-level current density, *Angew. Chem. Int. Ed.* 134 (2022) e202212329, <https://doi.org/10.1002/anie.202212329>.

[15] J. Gu, C.-S. Hsu, L. Bai, H.M. Chen, X. Hu, Atomically dispersed Fe³⁺ sites catalyze efficient CO₂ electroreduction to CO, *Science* 364 (2019) 1091–1094, <https://doi.org/10.1126/science.aaw7515>.

[16] J.R. Huang, X.F. Qiu, Z.H. Zhao, H.L. Zhu, Y.C. Liu, W. Shi, P.Q. Liao, X.M. Chen, Single-product faradaic efficiency for electrocatalytic of CO₂ to CO at current density larger than 1.2 A cm⁻² in neutral aqueous solution by a single-atom nanzyme, *Angew. Chem. Int. Ed.* 61 (2022) e202210985, <https://doi.org/10.1002/anie.202210985>.

[17] F.-Y. Gao, S.-J. Hu, X.-L. Zhang, Y.-R. Zheng, H.-J. Wang, Z.-Z. Niu, P.-P. Yang, R.-C. Bao, T. Ma, Z. Dang, Y. Guan, X.-S. Zheng, X. Zheng, J.-F. Zhu, M.-R. Gao, S.-H. Yu, High-curvature transition-metal chalcogenide nanostructures with a pronounced proximity effect enable fast and selective CO₂ electroreduction, *Angew. Chem. Int. Ed.* 59 (2020) 8706–8712, <https://doi.org/10.1002/anie.201912348>.

[18] D.M. Koshy, S. Chen, D.U. Lee, M.B. Stevens, A.M. Abdellah, S.M. Dull, G. Chen, D. Nordlund, A. Gallo, C. Hahn, D.C. Higgins, Z. Bao, T.F. Jaramillo, Understanding the origin of highly selective CO₂ electroreduction to CO on Ni, N-doped carbon catalysts, *Angew. Chem. Int. Ed.* 59 (2020) 4043–4050, <https://doi.org/10.1002/anie.201912857>.

[19] J.H. Lee, S. Kattel, Z. Jiang, Z. Xie, S. Yao, B.M. Tackett, W. Xu, N.S. Marinkovic, J. G. Chen, Tuning the activity and selectivity of electroreduction of CO₂ to synthesis gas using bimetallic catalysts, *Nat. Commun.* 10 (2019) 3724, <https://doi.org/10.1038/s41467-019-11352-0>.

[20] J. Chen, T. Wang, X. Wang, B. Yang, X. Sang, S. Zheng, S. Yao, Z. Li, Q. Zhang, L. Lei, J. Xu, L. Dai, Y. Hou, Promoting electrochemical CO₂ reduction via boosting activation of adsorbed intermediates on iron single-atom catalyst, *Adv. Funct. Mater.* 32 (2022) 2110174, <https://doi.org/10.1002/adfm.202110174>.

[21] J. Hao, Z. Zhuang, J. Hao, C. Wang, S. Lu, F. Duan, F. Xu, M. Du, H. Zhu, Interatomic electronegativity offset dictates selectivity when catalyzing the CO₂ reduction reaction, *Adv. Energy Mater.* 12 (2022) 2200579, <https://doi.org/10.1002/aenm.202200579>.

[22] Y. Li, X.F. Lu, S. Xi, D. Luan, X. Wang, X.W. Lou, Synthesis of N-doped highly graphitic carbon urchin-like hollow structures loaded with single-Ni atoms towards efficient CO₂ electroreduction, *Angew. Chem. Int. Ed.* 61 (2022) e202201491, <https://doi.org/10.1002/anie.202201491>.

[23] Y. Li, B. Wei, M. Zhu, J. Chen, Q. Jiang, B. Yang, Y. Hou, L. Lei, Z. Li, R. Zhang, Y. Lu, Synergistic effect of atomically dispersed Ni-Zn pair sites for enhanced CO₂ electroreduction, *Adv. Mater.* 33 (2021) 2102212, <https://doi.org/10.1002/adma.202102212>.

[24] X. Wei, S. Xiao, R. Wu, Z. Zhu, L. Zhao, Z. Li, J. Wang, J.S. Chen, Z. Wei, Activating COOH* intermediate by Ni/Ni₂Zn_{0.7} heterostructure in porous N-doped carbon nanofibers for boosting CO₂ electroreduction, *Appl. Catal. B* 302 (2022) 120861, <https://doi.org/10.1016/j.apcatb.2021.120861>.

[25] Y. Liu, H. Jiang, Z. Hou, Hidden mechanism behind the roughness-enhanced selectivity of carbon monoxide electrocatalytic reduction, *Angew. Chem. Int. Ed.* 60 (2021) 11133–11137, <https://doi.org/10.1002/anie.202016332>.

[26] T. Tang, Z. Wang, J. Guan, Optimizing the electrocatalytic selectivity of carbon dioxide reduction reaction by regulating the electronic structure of single-atom M-N-C materials, *Adv. Funct. Mater.* 32 (2022) 2111504, <https://doi.org/10.1002/adfm.202111504>.

[27] X. Li, S. Xi, L. Sun, S. Dou, Z. Huang, T. Su, X. Wang, Isolated FeN₄ sites for efficient electrocatalytic CO₂ reduction, *Adv. Sci.* 7 (2020) 2001545, <https://doi.org/10.1002/advs.202001545>.

[28] D. Xi, J. Li, J. Low, K. Mao, R. Long, J. Li, Z. Dai, T. Shao, Y. Zhong, Y. Li, Z. Li, X. J. Loh, L. Song, E. Ye, Y. Xiong, Limiting the uncoordinated N species in M-N_x single-atom catalysts toward electrocatalytic CO₂ reduction in broad voltage range, *Adv. Mater.* 34 (2022) 2104090, <https://doi.org/10.1002/adma.202104090>.

[29] X. Cao, L. Zhao, B. Wulan, D. Tan, Q. Chen, J. Ma, J. Zhang, Atomic bridging structure of nickel-nitrogen-carbon for highly efficient electrocatalytic reduction of CO₂, *Angew. Chem. Int. Ed.* 61 (2022) e202113918, <https://doi.org/10.1002/anie.202113918>.

[30] H. Guo, D.-H. Si, H.-J. Zhu, Q.-X. Li, Y.-B. Huang, R. Cao, Ni single-atom sites supported on carbon aerogel for highly efficient electroreduction of carbon dioxide with industrial current densities, *eScience* 2 (2022) 295–303, <https://doi.org/10.1016/j.esci.2022.03.007>.

[31] Y. Li, S.L. Zhang, W. Cheng, Y. Chen, D. Luan, S. Gao, X.W. Lou, Loading single-Ni atoms on assembled hollow N-rich carbon plates for efficient CO₂ electroreduction, *Adv. Mater.* 34 (2022) 2105204, <https://doi.org/10.1002/adma.202105204>.

[32] S. Chen, X. Li, C.-W. Kao, T. Luo, K. Chen, J. Fu, C. Ma, H. Li, M. Li, T.-S. Chan, M. Liu, Unveiling the proton-feeding effect in sulfur-doped Fe-N-C single-atom catalyst for enhanced CO₂ electroreduction, *Angew. Chem. Int. Ed.* 61 (2022) e202206233, <https://doi.org/10.1002/anie.202206233>.

[33] L. Jiao, H. Yan, Y. Wu, W. Gu, C. Zhu, D. Du, Y. Lin, When nanzymes meet single-atom catalysis, *Angew. Chem. Int. Ed.* 59 (2020) 2565–2576, <https://doi.org/10.1002/anie.201905645>.

[34] J.A. Trindell, J. Clausmeyer, R.M. Crooks, Size stability and H₂/CO selectivity for Au nanoparticles during electrocatalytic CO₂ reduction, *J. Am. Chem. Soc.* 139 (2017) 16161–16167, <https://doi.org/10.1021/jacs.7b06775>.

[35] Q. Hu, Z. Han, X. Wang, G. Li, Z. Wang, X. Huang, H. Yang, X. Ren, Q. Zhang, J. Liu, C. He, Facile synthesis of sub-nanometric copper clusters by double confinement enables selective reduction of carbon dioxide to methane, *Angew. Chem. Int. Ed.* 59 (2020) 19054–19059, <https://doi.org/10.1002/anie.202009277>.

[36] X. Zhang, C. Liu, Y. Zhao, L. Li, Y. Chen, F. Raziq, L. Qiao, S.-X. Guo, C. Wang, G. G. Wallace, A.M. Bond, J. Zhang, Atomic nickel cluster decorated defect-rich copper for enhanced C₂ product selectivity in electrocatalytic CO₂ reduction, *Appl. Catal. B* 291 (2021) 120030, <https://doi.org/10.1016/j.apcatb.2021.120030>.

[37] Q. Chang, J.H. Lee, Y. Liu, Z. Xie, S. Hwang, N.S. Marinkovic, A.A. Park, S. Kattel, J.G. Chen, Electrochemical CO₂ reduction reaction over Cu nanoparticles with tunable activity and selectivity mediated by functional groups in polymeric binder, *J. Am. Chem. Soc.* 2 (2022) 214–222, <https://doi.org/10.1021/jacsau.1c00487>.

[38] M. Abdinejad, E. Irtem, A. Farzi, M. Sassenburg, S. Subramanian, H.-P. Iglesias van Montfort, D. Ripepi, M. Li, J. Middelkoop, A. Seifitokaldani, T. Burdny, CO₂ electrolysis via surface-engineering electrografted pyridines on silver catalysts, *ACS Catal.* 12 (2022) 7862–7876, <https://doi.org/10.1021/acscatal.2c01654>.

[39] Z. Cao, D. Kim, D. Hong, Y. Yu, J. Xu, S. Lin, X. Wen, E.M. Nichols, K. Jeong, J. A. Reimer, P. Yang, C.J. Chang, A molecular surface functionalization approach to tuning nanoparticle electrocatalysts for carbon dioxide reduction, *J. Am. Chem. Soc.* 138 (2016) 8120–8125, <https://doi.org/10.1021/jacs.6b02878>.

[40] S. Jin, Z. Hao, K. Zhang, Z. Yan, J. Chen, Advances and challenges for the electrochemical reduction of CO₂ to CO: From fundamentals to industrialization, *Angew. Chem. Int. Ed.* 60 (2021) 20627–20648, <https://doi.org/10.1002/anie.202101818>.

[41] X. Wang, P. Ou, J. Wicks, Y. Xie, Y. Wang, J. Li, J. Tam, D. Ren, J.Y. Howe, Z. Wang, A. Ozden, Y.Z. Finrock, Y. Xu, Y. Li, A.S. Rasouli, K. Bertens, A.H. Ip, M. Graetzel, D. Sinton, E.H. Sargent, Gold-in-copper at low *CO coverage enables efficient electromethanation of CO₂, *Nat. Commun.* 12 (2021) 3387, <https://doi.org/10.1038/s41467-021-23699-4>.

[42] Y. Zhao, X. Tan, W. Yang, C. Jia, X. Chen, W. Ren, S.C. Smith, C. Zhao, Surface reconstruction of ultrathin palladium nanosheets during electrocatalytic CO₂ reduction, *Angew. Chem. Int. Ed.* 59 (2020) 21493–21498, <https://doi.org/10.1002/anie.202009616>.

[43] X. Deng, D. Alfonso, T.-D. Nguyen-Phan, D.R. Kauffman, Resolving the size-dependent transition between CO₂ reduction reaction and H₂ evolution reaction selectivity in sub-5 nm silver nanoparticle electrocatalysts, *ACS Catal.* 12 (2022) 5921–5929, <https://doi.org/10.1021/acscatal.2c00960>.

[44] S. Li, W. Chen, X. Dong, C. Zhu, A. Chen, Y. Song, G. Li, W. Wei, Y. Sun, Hierarchical micro/nanostructured silver hollow fiber boosts electroreduction of carbon dioxide, *Nat. Commun.* 13 (2022) 3080, <https://doi.org/10.1038/s41467-022-30733-6>.

[45] X. Wu, Y. Guo, Z. Sun, F. Xie, D. Guan, J. Dai, F. Yu, Z. Hu, Y.C. Huang, C.W. Pao, J. L. Chen, W. Zhou, Z. Shao, Fast operando spectroscopy tracking in situ generation of rich defects in silver nanocrystals for highly selective electrochemical CO₂ reduction, *Nat. Commun.* 12 (2021) 660, <https://doi.org/10.1038/s41467-021-20960-8>.

[46] J. Chen, X. Liu, S. Xi, T. Zhang, Z. Liu, J. Chen, L. Shen, S. Kawi, L. Wang, Functionalized Ag with thiol ligand to promote effective CO₂ electroreduction, *ACS Nano* 16 (2022) 13982–13991, <https://doi.org/10.1021/acsnano.2c03512>.

[47] H.Q. Fu, J. Liu, N.M. Bedford, Y. Wang, J.W. Sun, Y. Zou, M. Dong, J. Wright, H. Diao, P. Liu, H.G. Yang, H. Zhao, Synergistic Cr₂O₃@Ag heterostructure

enhanced electrocatalytic CO₂ reduction to CO, *Adv. Mater.* 34 (2022) 2202854, <https://doi.org/10.1002/adma.202202854>.

[48] S. Liu, X.-Z. Wang, H. Tao, T. Li, Q. Liu, Z. Xu, X.-Z. Fu, J.-L. Luo, Ultrathin 5-fold twinned sub-25nm silver nanowires enable highly selective electroreduction of CO₂ to CO, *Nano Energy* 45 (2018) 456–462, <https://doi.org/10.1016/j.nanoen.2018.01.016>.

[49] S. Liu, C. Sun, J. Xiao, J.-L. Luo, Unraveling structure sensitivity in CO₂ electroreduction to near-unity CO on silver nanocubes, *ACS Catal.* 10 (2020) 3158–3163, <https://doi.org/10.1021/acscatal.9b03883>.

[50] C. Zhao, X. Dai, T. Yao, W. Chen, X. Wang, J. Wang, J. Yang, S. Wei, Y. Wu, Y. Li, Ionic exchange of metal-organic frameworks to access single nickel sites for efficient electroreduction of CO₂, *J. Am. Chem. Soc.* 139 (2017) 8078–8081, <https://doi.org/10.1021/jacs.7b02736>.

[51] W. Xiong, H. Li, H. Wang, J. Yi, H. You, S. Zhang, Y. Hou, M. Cao, T. Zhang, R. Cao, Hollow mesoporous carbon sphere loaded Ni-N₄ single-atom: support structure study for CO₂ electrocatalytic reduction catalyst, *Small* 16 (2020) 2003943, <https://doi.org/10.1002/smll.202003943>.

[52] R. Daiyan, X. Zhu, Z. Tong, L. Gong, A. Razmjou, R.-S. Liu, Z. Xia, X. Lu, L. Dai, R. Amal, Transforming active sites in nickel-nitrogen-carbon catalysts for efficient electrochemical CO₂ reduction to CO, *Nano Energy* 78 (2020) 105213, <https://doi.org/10.1016/j.nanoen.2020.105213>.

[53] S. Liu, H.B. Yang, S.F. Hung, J. Ding, W. Cai, L. Liu, J. Gao, X. Li, X. Ren, Z. Kuang, Y. Huang, T. Zhang, B. Liu, Elucidating the electrocatalytic CO₂ reduction reaction over a model single-atom nickel catalyst, *Angew. Chem. Int. Ed.* 59 (2020) 798–803, <https://doi.org/10.1002/anie.201911995>.

[54] G. Kresse, J. Furthmüller, Efficiency of ab-initio total energy calculations for metals and semiconductors using a plane-wave basis set, *Comput. Mater. Sci.* 6 (1996) 15–50, [https://doi.org/10.1016/0927-0256\(96\)00008-0](https://doi.org/10.1016/0927-0256(96)00008-0).

[55] G. Kresse, J. Furthmüller, Efficient iterative schemes for ab initio total-energy calculations using a plane-wave basis set, *Phys. Rev. B* 54 (1996) 11169, <https://link.aps.org/doi/10.1103/PhysRevB.54.11169>.

[56] J.P. Perdew, K. Burke, M. Ernzerhof, Generalized gradient approximation made simple, *Phys. Rev. Lett.* 77 (1996) 3865, <https://link.aps.org/doi/10.1103/PhysRevLett.77.3865>.

[57] G. Kresse, D. Joubert, From ultrasoft pseudopotentials to the projector augmented-wave method, *Phys. Rev. B* 59 (1999) 1758, <https://link.aps.org/doi/10.1103/PhysRevB.59.1758>.

[58] S. Grimme, Semiempirical GGA-type density functional constructed with a long-range dispersion correction, *J. Comput. Chem.* 27 (2006) 1787–1799, <https://doi.org/10.1002/jcc.20495>.

[59] Y.-C. Hsieh, S.D. Senanayake, Y. Zhang, W. Xu, D.E. Polanyik, Effect of chloride anions on the synthesis and enhanced catalytic activity of silver nanocoral electrodes for CO₂ electroreduction, *ACS Catal.* 5 (2015) 5349–5356, <https://doi.org/10.1021/acscatal.5b01235>.

[60] L. Fan, P.F. Liu, X. Yan, L. Gu, Z.Z. Yang, H.G. Yang, S. Qiu, X. Yao, Atomically isolated nickel species anchored on graphitized carbon for efficient hydrogen evolution electrocatalysis, *Nat. Commun.* 7 (2016) 10667, <https://doi.org/10.1038/ncomms10667>.

[61] C. Yan, H. Li, Y. Ye, H. Wu, F. Cai, R. Si, J. Xiao, S. Miao, S. Xie, F. Yang, Y. Li, G. Wang, X. Bao, Coordinatively unsaturated nickel-nitrogen sites towards selective and high-rate CO₂ electroreduction, *Energy Environ. Sci.* 11 (2018) 1204–1210, <https://doi.org/10.1039/C8EE00133B>.

[62] Y.N. Gong, L. Jiao, Y. Qian, C.Y. Pan, L. Zheng, X. Cai, B. Liu, S.H. Yu, H.L. Jiang, Regulating the coordination environment of mOF-templated single-atom nickel electrocatalysts for boosting CO₂ reduction, *Angew. Chem. Int. Ed.* 59 (2020) 2705–2709, <https://doi.org/10.1002/anie.201914977>.

[63] L. Jiao, W. Yang, G. Wan, R. Zhang, X. Zheng, H. Zhou, S.-H. Yu, H.-L. Jiang, Single-atom electrocatalysts from multivariate metal-organic frameworks for highly selective reduction of CO₂ at low pressures, *Angew. Chem. Int. Ed.* 59 (2020) 20589–20595, <https://doi.org/10.1002/anie.202008787>.

[64] P. Chen, T. Zhou, L. Xing, K. Xu, Y. Tong, H. Xie, L. Zhang, W. Yan, W. Chu, C. Wu, Y. Xie, Atomically dispersed iron-nitrogen species as electrocatalysts for bifunctional oxygen evolution and reduction reactions, *Angew. Chem. Int. Ed.* 56 (2017) 610–614, <https://doi.org/10.1002/anie.201610119>.

[65] C. Wang, X. Hu, X. Hu, X. Liu, Q. Guan, R. Hao, Y. Liu, W. Li, Typical transition metal single-atom catalysts with a metal-pyridine N structure for efficient CO₂ electroreduction, *Appl. Catal. B* 296 (2021) 120331, <https://doi.org/10.1016/j.apcatb.2021.120331>.

[66] Z. Geng, Y. Cao, W. Chen, X. Kong, Y. Liu, T. Yao, Y. Lin, Regulating the coordination environment of Co single atoms for achieving efficient electrocatalytic activity in CO₂ reduction, *Appl. Catal. B* 240 (2019) 234–240, <https://doi.org/10.1016/j.apcatb.2018.08.075>.

[67] S. Liu, H. Tao, L. Zeng, Q. Liu, Z. Xu, Q. Liu, J.-L. Luo, Shape-dependent electrocatalytic reduction of CO₂ to CO on triangular silver nanoplates, *J. Am. Chem. Soc.* 139 (2017) 2160–2163, <https://doi.org/10.1021/jacs.6b12103>.